Journal of Solid State Chemistry 181 (2008) 2243–2249

Contents lists available at ScienceDirect

Journal of Solid State Chemistry

journal homepage: www.elsevier.com/locate/jssc

Phase formation, structural and microstructural characterization of novel oxynitride–perovskites synthesized by thermal ammonolysis of (Ca,Ba)MoO_4 and (Ca,Ba)MoO_3

D. Logvinovich [a], M.H. Aguirre [a], J. Hejtmanek [b], R. Aguiar [c], S.G. Ebbinghaus [c], A. Reller [c], A. Weidenkaff [a,*]

[a] Solid State Chemistry and Catalysis, Empa, Ueberlandstr. 129, CH-8600 Duebendorf, Switzerland
[b] Institute of Physics, ASCR, Cukrovarnická 10, CZ-15263, Prague 6, Czech Republic
[c] Lehrstuhl für Festkörperchemie, Institut für Physik, Universität Augsburg, Universitätsstrasse 1, D-86159, Augsburg, Germany

ARTICLE INFO

Article history:
Received 5 February 2008
Received in revised form
26 April 2008
Accepted 1 May 2008
Available online 16 May 2008

Keywords:
Oxynitride
Molybdate
Crystal structure

ABSTRACT

Reactions of $AMoO_4$ and $AMoO_3$ ($A = Ca^{2+}$, Ba^{2+}) with ammonia were investigated at 873 K < T < 1123 K with the particular intention to synthesize novel oxynitride–perovskites of the general composition $AMo(O,N)_3$ and to study their crystal structure. $CaMo(O,N)_3$ and $BaMo(O,N)_3$ were prepared by thermal ammonolysis of the corresponding $CaMoO_3$ and $BaMoO_3$ precursors at $T = 898$ and 998 K, respectively. The structural parameters of the oxynitrides were obtained from Rietveld refinements of X-ray and neutron powder diffraction data. $CaMo(O,N)_3$ crystallizes in the $GdFeO_3$ distorted perovskite structure with orthorhombic space group *Pbnm* and $a = 5.5029(1)$ Å, $b = 5.5546(1)$ Å, $c = 7.8248(1)$ Å as determined by X-ray powder diffraction. Its O/N content refined from the neutron diffraction data corresponds to the composition $CaMoO_{1.7(1)}N_{1.3(1)}$. $BaMo(O,N)_3$ crystallizes in the cubic perovskite structure with space group $Pm\bar{3}m$ and $a = 4.0657(1)$ Å as determined by X-ray powder diffraction. Transmission electron microscopy reveals a complex microstructure for both $CaMoO_3$ and $CaMoO_{1.7(1)}N_{1.3(1)}$ represented by twin domains of different orientation.

1. Introduction

The interest on N^{3-}- and N_2-containing inorganic and metal-organic Mo derivatives is driven by the ability of these compounds to catalyze molecular nitrogen reduction into ammonia [1,2]. Therefore, oxynitride–perovskites and intermediate products of their thermal reoxidation [3] are potentially interesting materials to be tested for this application. Oxyntrides are normally prepared by thermally activated reactions between ternary oxides like ABO_4, $A_2B_2O_7$ ($A = RE$, AE; B = transition element) or oxides–carbonates mixtures (B_xO_y–$A_n(CO_3)_m$) with B-site cation in its stable oxidation state and ammonia [4–7]. Oxide and oxide–carbonate precursors were successfully applied to prepare a number of Ti^{4+}, Ta^{5+}, Nb^{5+}-containing oxynitride–perovskite phases $AB(O,N)_3$ [7–10]. The only known molybdenum based oxynitride–perovskite system is $SrMoO_{3-x}N_x$ [9,11,12]. It was prepared by thermal ammonolysis of $SrMoO_4$ with Mo in its air-stable formal oxidation state +6, at $T = 1023$ –1073 K. In $SrMoO_{3-x}N_x$ the formal oxidation state of molybdenum varies between +4 and +6 depending on the anionic composition. Interestingly, although the perovskite-type oxides $CaMoO_3$ and $BaMoO_3$ are known [13–16], no reports on the synthesis of the corresponding oxynitrides are available in the literature. One reported attempt to prepare $BaMo(O,N)_3$ by thermal ammonolysis of $BaMoO_4$ led to a mixture of $BaMoO_3$ and $Ba_3Mo_2O_6N$ [11].

The lack of Mo-containing oxynitride–perovskite phases motivated us to investigate whether $CaMo(O,N)_3$ and $BaMo(O,N)_3$ can be prepared by thermal ammonolysis and, if yes, to study and compare their crystal structures with those of the corresponding oxides $CaMoO_3$ and $BaMoO_3$.

Two different series of oxides, namely $AMo^{6+}O_4$ and its reduced form $AMo^{4+}O_3$ ($A = Ca^{2+}$, Ba^{2+}), have been chosen as precursors to find out whether the structure of the starting compound has an influence on the phase formation during the ammonolysis at different temperatures.

2. Experimental

$BaMoO_4$ was prepared according to the procedure described in [17]. A 0.1 M solution of $Ba(NO_3)_2$ (Merck, purity >99.0%) was poured slowly with constant stirring into a 0.1 M solution of Na_2MoO_4 (Riedel-de Haän, purity >99.5%). The formed

* Corresponding author.
E-mail address: anke.weidenkaff@empa.ch (A. Weidenkaff).

0022-4596/$ - see front matter © 2008 Elsevier Inc. All rights reserved.
doi:10.1016/j.jssc.2008.05.012

precipitate was washed several times with deionised water and calcined at 1073 K during 4 h.

$BaMoO_3$ was obtained by reduction of $BaMoO_4$ (1 g) with a forming gas (5% of H_2 in N_2) flow of 300 mL/min. The reduction was carried out at $T = 1473$ K during 15 h in a tubular quartz reactor with an internal diameter of 30 mm.

$CaMoO_4$ was synthesized by the citrate precursor method [14]. Stoichiometric amounts of $H_{24}Mo_7N_6O_{24}{}^*4H_2O$ (Fluka, >99.0%) and $CaCO_3$ (Alfa Aesar, >99.5%) were dissolved in an aqueous 0.1 M citric acid $C_6H_8O_7$ (Riedel-de Haän, >99.5%) solution. The amount of citric acid was 3 times the total molar amount of Mo and Ca. The obtained solution was predried at 393 K overnight and heated up to 873 K within 12 h. The final product was then heated from 873 K to 1073 K with a heating rate of 5 K/min, calcined at that temperature during 2 h and cooled down to room temperature.

$CaMoO_3$ was synthesized by reduction of $CaMoO_4$ produced by the citrate method with forming gas (5% of H_2 in N_2). [14] The reduction of 1 g of $CaMoO_4$ was carried out at 1173 K during 12 h (with an intermediate regrinding after 4 and 8 h of the reaction) under a forming gas flow of 100–300 mL/min in a quartz reactor with an internal diameter of 30 mm. [18] Forming gas was supplied through a quartz tube with a diameter of 5.8 mm placed above the sample and about 2 mm from the reactor end. After the reaction, the sample was quenched down to room temperature within 1 min.

All the synthesized oxides were reacted with ammonia gas (PanGas, 99.999%, 100 mL/min) at $873\ K < T < 1123$ K. The reactions were carried out at T interval of 25 K in an Al_2O_3 reactor with an internal diameter of 30 mm. Each sample load was 0.1 g. The reaction time was 20 h. Ammonia was supplied by means of a quartz tube with a diameter 5.8 mm placed above the sample. Heating and cooling rates were 10 K/min.

Structure and phase purity of the starting and reacted powders were studied by X-ray powder diffraction (XRPD) using a Phillips X'Pert PRO MPD Θ–Θ System equipped with a linear X'Celerator detector. Crystallographic parameters were obtained from Rietveld refinement of the XRPD data, recorded in the 2Θ angular range of 20–140° with a step size of 0.02° and a counting time of 20 s/step. A proportional counter was used to detect scattered X-rays. The reflection shape was modeled with a Thompson–Cox–Hastings (TCH) pseudo-Voigt profile function [19] corrected for asymmetry. [20,21] Employing that function allows to extract the samples intrinsic profile by using the known instrumental profile and performing a line broadening analysis to conclude about particle size and strain. [22] The instrumental profile was obtained from the measurement of LaB_6 SRM 660a standard.

Neutron diffraction (ND) data were recorded at the high-resolution powder diffractometer for thermal neutrons [23] located at the Swiss Spallation Neutron Source (SINQ) of the Paul Scherrer Institute in Switzerland. Samples were placed in cylindrical vanadium cans with 6 mm in diameter. The measurements were performed with a neutron wavelength of $\lambda = 1.494$ Å in the angular range of 4.5–165° with a step size of 0.05°. The reflection shape was modeled using a TCH pseudo-Voigt profile function. All the refinements were performed using Fullprof [24].

The O/N content of the different samples was measured by the hotgas-extraction method using a LECO TC500 analyzer. Silicon nitride and silicon oxide were used as calibration standards for nitrogen and oxygen, respectively.

Electron diffraction (ED) studies were done by transmission electron microscopy (TEM) using a Philips CM30 microscope operating at 300 kV. Diffraction simulations were performed using JEMS [25].

3. Results and discussion

XRPD confirmed phase purity of all the synthesized oxides, except $CaMoO_3$, for which an Mo impurity of 2.3 weight% was refined. Crystallographic parameters of $CaMoO_3$ as obtained by refinement of the XRPD data in space group *Pbnm* are summarized in Tables 1 and 2 and are in good agreement with a previous ND study of this compound [14]. The observed isotropic line broadening was accounted for by refining isotropic size-strain components (in Fullprof referred to as U and Y) of the sample intrinsic profile. Their refined values correspond to an apparent size value of 0.13 μm and an apparent strain value of 0.31%.

The refined lattice parameter of $BaMoO_3$ is equal to 4.0409(1) Å, which is close to the value of 4.0404(3) Å reported in Ref. [15]. No line broadening was found for this oxide with respect to the used standard LaB_6.

Both $CaMoO_3$ and $BaMoO_3$ are of a purple-red color. In contact with moisture they oxidize slowly (within several hours/days) into corresponding $CaMoO_4$ and $BaMoO_4$. Therefore, they were stored under dry nitrogen atmosphere.

Reflections corresponding to $Ba_3Mo_2O_6N_2$ [26,27] and $BaMoO_4$ are identified for the $BaMoO_4$ sample reacted at 898 K for 20 h. The $BaMoO_4$ main reflections disappear upon heating the sample up to 973 K. XRPD confirms $Ba_3Mo_2O_6N_2$ to be the main phase formed after the ammonolysis at $T = 973$ K.

Table 1
Refinement results for $CaMoO_3$ and $CaMoO_{1.7(1)}N_{1.3(1)}$

Name		$CaMoO_3$	$CaMoO_{1.7(1)}N_{1.3(1)}$	$CaMoO_{1.7(1)}N_{1.3(1)}$
Radiation		X-ray Cu$K_{\alpha 1/2}$	X-ray Cu$K_{\alpha 1/2}$	Neutron (HRPT, PSI)
λ, Å		1.5406/1.5444	1.5406/1.5444	1.494
T, K		298	298	298
S,G		*Pbnm*	*Pbnm*	*Pbnm*
a, Å		5.4499(1)	5.5029(1)	5.5068(1)
b, Å		5.5811(1)	5.5546(1)	5.5593(1)
c, Å		7.7791(1)	7.8248(1)	7.8317(2)
V, Å^3		236.62(1)	239.19(1)	239.76(1)
Z		4	4	4
Ca	x	0.9894(7)	0.997(1)	0.994(1)
	y	0.0461(3)	0.0294(5)	0.0334(9)
	z	1/4	1/4	1/4
	B_{iso}, Å^2	0.46(4)	1.13(3)	1.05(7)
	Site	4*c*	4*c*	4*c*
	Occ.	1	1	1
Mo	x	1/2	1/2	1/2
	y	0	0	0
	z	0	0	0
	B_{iso}, Å^2	0.11(2)	0.90(1)	0.74(5)
	Site	4*b*	4*b*	4*b*
	Occ.	1	1	1
O/N(1)	x	0.081(1)	0.072(1)	0.0642(6)
	y	0.475(1)	0.473(2)	0.4872(7)
	z	1/4	1/4	1/4
	B_{iso}, Å^2	0.92(7)	1.13(9)	0.90(8)
	Site	4*c*	4*c*	4*c*
	Occ.	1/0	0.56/0.44[a]	0.56(4)/0.44(4)
O/N(2)	x	0.7055(8)	0.703(1)	0.7113(5)
	y	0.2921(8)	0.290(1)	0.2885(5)
	z	0.0453(6)	0.0329(9)	0.0329(3)
	B_{iso}, Å^2	0.92(7)	1.13(9)	0.90(6)
	Site	8*d*	8*d*	8*d*
	Occ.	1/0	0.57/0.43[a]	0.57(3)/0.43(3)
χ^2		2.13	1.71	1.97
wR_p^b		0.135	0.136	0.128
R_p^b		0.102	0.128	0.149

[a] Not refined.

Table 2
Selected bond distances in Å and angles in degrees calculated for $CaMoO_3$ and $CaMoO_{1.7(1)}N_{1.3(1)}$[a]

		$CaMoO_3$	$CaMoO_{1.7(1)}N_{1.3(1)}$
Mo–O/N(1)	x2	2.000(1)	1.9909(6)
Mo–O/N(2)	x2	2.009(4)	1.997(3)
Mo–O/N(2)	x2	2.012(4)	1.995(3)
⟨Mo–O/N⟩		2.007(3)	1.994(2)
Ca–O/N(1)		3.228(6)	3.061(6)
Ca–O/N(1)		2.445(6)	2.552(6)
Ca–O/N(1)		3.138(7)	3.085(8)
Ca–O/N(1)		2.371(7)	2.446(8)
Ca–O/N(2)	x2	2.610(5)	2.708(6)
Ca–O/N(2)	x2	2.735(5)	2.705(5)
Ca–O/N(2)	x2	2.382(5)	2.454(5)
Ca–O/N(2)	x2	3.407(5)	3.278(5)
$\langle Ca–O/N\rangle_{(8\ short)}$[b]		2.520(6)	2.592(6)
Mo–O/N(1)–Mo	x2	153.00(6)	159.13(3)
Mo–O/N(2)–Mo	x4	151.9(2)	157.0(1)
⟨Mo–O/N–Mo⟩		152.27(1)	157.72(8)

[a] Derived from the neutron data.
[b] The average, calculated from the 8 shortest distances.

Some additional reflections belonging to a phase, indexed as a cubic perovskite with the lattice parameter larger than that of $BaMoO_3$ are also resolved. These reflections are attributed to a nitrided $BaMoO_3$ (further referred to as $BaMo(O,N)_3$). The reflections of this phase disappear after 40 h of the ammonolysis at $T = 973$ K; after that only reflections of $Ba_3Mo_2O_6N_2$ can be resolved. In the XRPD pattern of the sample which was reacted with ammonia at 1023 K Mo_2N and $Ba_3Mo_2O_6N_2$ are the main identified phases. Two weak reflections, which belong to an unidentifiable phase, appear between the (015) and (110) reflections of $Ba_3Mo_2O_6N_2$. Thus, $BaMo(O,N)_3$ is not formed as a main phase from $BaMoO_4$ under the chosen reaction conditions.

The reaction between $CaMoO_4$ and ammonia starts at 873 K. The XRPD patterns reveal the appearance of broad features coincident with the main reflections of Mo_2N [28]. At 898 K CaO and Mo_2N can be identified. Some additional reflections that could not be assigned to any known phase appear at that temperature. The XRPD pattern of the sample reacted with NH_3 at higher temperatures reveals the presence of the CaO and Mo_2N. Thus, $CaMo(O,N)_3$ cannot be prepared directly from $CaMoO_4$ under the chosen reaction conditions.

A noticeable interaction between $CaMoO_3$ (Fig. 1A) and NH_3 starts at 898 K. The ammonolysis results in a perovskite-type phase with cell parameters deviating from the ones of the starting oxide. Its formation can best be monitored by inspection of the (200), (020) and (002) located roughly between 32° and 33° 2θ. During the reaction the (002) and (200) reflections are shifted to lower angles, whereas the (020) reflection is shifted to higher angles. This indicates an increase in a and c, but a decrease in the b parameter of the unit cell due to the progressive enrichment of the material with nitrogen. As can be seen from Fig. 1B a broadening of the diffraction peaks occurs in the early stages of the ammonolysis. A closer examination reveals the splitting of the reflections (see the inset of Fig. 1B). At that stage the pattern can be fitted assuming two perovskite-type phases (*Pbnm*) of different lattice parameters and atomic coordinates, corresponding to $CaMo(O,N)_3$ samples with different anionic composition. The kinetics of oxygen exchange with nitrogen is slow due to the low synthesis temperature. The rate of the oxynitride phase formation enhances with increasing temperature, increasing ammonia flow and/or decreasing sample mass. The oxynitride phase formed (Fig. 1C) is stable under ammonia up to $T = 923$ K. A further increase of temperature leads to the formation of Mo_2N and CaO impurities.

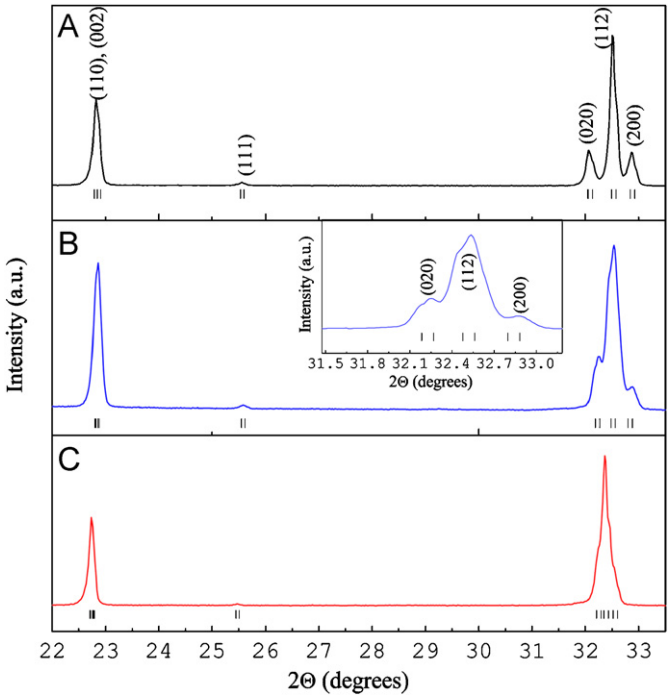

Fig. 1. Evolution of the XRPD profile with time measured during the ammonolysis of $CaMoO_3$ at $T = 898$ K. (A) Non-reacted sample; (B) The sample after the 50 h reaction (the inset shows the splitting of the main reflections due to the non-uniform O/N distribution through the particles depth); (C) The sample after the 100 h reaction.

The sample batch used for the crystallographic investigation by Rietveld refinements was obtained by ammonolysing 0.7 g of $CaMoO_3$ at $T = 898$ K during 100 h (when the main reflections splitting disappeared and no further change in the lattice parameters was detected by XRPD) under an ammonia flow of 300 mL/min. After the reaction the sample was quenched to room temperature within 1 min. Increasing the synthesis temperature to $T > 898$ K led to the oxynitride phase with lower nitrogen content as deduced from the Bragg reflection positions measured by XRPD. The explanation for this is given further in the text.

The ammonolysis of $BaMoO_3$ (Fig. 2A) proceeds similar to that of $CaMoO_3$. The temperature had to be raised up to 998 K and the sample mass had to be decreased down to 0.25 g in order to promote a faster formation of the oxynitride phase. As in case of the $CaMoO_3$ ammonolysis, a broadening of the perovskite-phase reflections and their shift to lower angles is observed. This indicates the formation of the oxynitride–perovskite phase $BaMo(O,N)_3$ with a larger lattice constant compared to $BaMoO_3$. However, the formation of the secondary phases is simultaneously observed (Fig. 2B). Some of the reflections were assigned to Mo, BaO and $Ba_3Mo_2O_6N_2$ phases. However, we could not attribute the main impurity phase reflections, which are coincident with those of the phase formed during the ammonolysis of $BaMoO_4$ at 1023 K, to any phase of the Ba–Mo–O–N system found in ICSD (inorganic crystal structure database) and Pdf-2 (powder diffraction files) databases. Therefore, we conclude that they belong to a previously undiscovered phase of the Ba–Mo–O–N system. The broadening of $BaMo(O,N)_3$ reflections decreases with time. It has to be noted that while the ammonolysis of $BaMoO_4$ leads to the minor amount of the $BaMo(O,N)_3$ phase, the ammonolysis of $BaMoO_3$ leads to a considerable $BaMo(O,N)_3$ yield.

Both $CaMo(O,N)_3$ and $BaMo(O,N)_3$ possess a dark blue color. The materials are moisture sensitive. Therefore, they

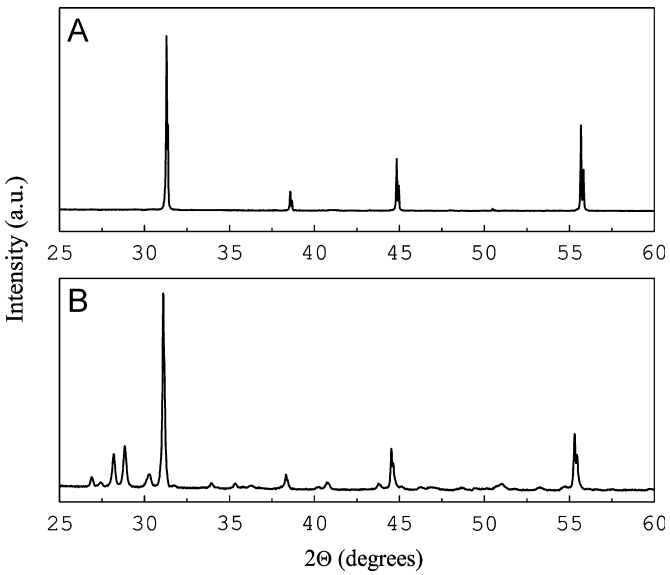

Fig. 2. Thermal ammonolysis study of $BaMoO_3$. (A) Pure $BaMoO_3$; (B) The sample reacted with NH_3 at $T = 998$ K during 85 h (the shift of the perovskite phase reflections to lower angles can be seen).

were stored under the same conditions as $CaMoO_3$ and $BaMoO_3$.

During its reactions with $AMoO_3$ and $AMoO_4$ oxides, NH_3 can act as a nitriding and a reducing agent:

$$AMoO_{4(s)} + (2+2x)/3NH_{3(g)} = AMoO_{3-x(s)}N_x + (1+x)\,H_2O_{(g)} + (2-x)/6N_{2(g)} \text{ (reduction)}$$

$$AMoO_{3-x(s)} + yNH_{3(g)} = AMoO_{3-x-y}N_{x+y(s)} + yH_2O_{(g)} + yH_2O_{(g)} + (y/2)H_{2(g)} \text{ (nitridation)}$$

At $T > 573$ K ammonia undergoes considerable dissociation :

$$2NH_{3(g)} = N_{2(g)} + 3H_{2(g)}$$

The formed hydrogen can also further reduce $AMoO_4/AMoO_3$. Depending on the relative rates of the processes described above, a more nitrided or more reduced product will be formed. As mentioned in Ref. [4] the dissociation of ammonia should be minimized before it reaches the sample's surface to achieve the most effective nitridation conditions. Otherwise the reduction may dominate over the nitridation reaction. That is why it is important to increase the ammonia flow with temperature [4]. Additionally, increasing ammonia flow promotes faster water removal [29,30] and the renewal of active nitriding species over the sample. These factors can account for the enhanced kinetics of the oxynitride phase formation observed during the ammonolysis of $AMoO_3$ when increasing the ammonia flow. Partial dissociation of ammonia at elevated temperature before reaching the sample's surface explains the observed formation of the $CaMo(O,N)_3$ oxynitride phase with lower nitrogen content.

Besides the ammonia flow rate, the structure of the starting precursor and the ionic radius of the *A*-site cation as well as the covalence of the Mo–(O/N) bonding have an influence on the oxynitride phase formation.

A detailed study on the Mo oxidation state stability of $AMoO_4$ and $AMoO_3$ (A = Ca, Sr, Ba) against reduction is available from the work of Kamata et al. [13,16]. The authors reported that the alkaline-earth cation with a larger ionic radius provides better stabilization of the Mo-oxidation state in $AMoO_3$ and $AMoO_4$. The influence of the *A*-site cation ionic radius on the Mo-oxidation state stability was discussed in terms of the positive inductive effect. Strength of the positive inductive effect of a cation is related with its polarizing power [31]. The latter is inversely proportional to the ionic radius of the cation. Hence, within one group of the Periodic Table the strength of the positive inductive effect decreases with decreasing the ionic radius of the element. Thus, for Ca^{2+}, Sr^{2+} and Ba^{2+} the strength of the positive inductive effect decreases with the sequence $Ba^{2+} > Sr^{2+} > Ca^{2+}$. In the same sequence the ability of the alkaline-earth ion to retain the Mo-ions oxidation state decreases. Indeed, during the ammonolysis of $AMoO_4$ the increase of the Mo-oxidation state in the main product phase with the increase of the *A*-site cation ionic radius is observed.

Apart from the ammonia flow rate and the positive inductive effect, other parameters such as the influence of the lattice energy and structure distortion energy on the phase formation during the ammonolysis have to be considered.

Apparently, $AMoO_3$ undergoes fewer structural changes during the ammonolysis than $AMoO_4$. The lattice stability of $AMoO_3$ is higher than that of $AMoO_4$. This is the most probable explanation for the differences in the phase formation observed during the ammonolysis of $AMoO_4$ and $AMoO_3$ (with equal *A*-site cation).

The tolerance factor (t) expresses the degree of distortion of the perovskite structure (ABX_3). It is calculated by dividing the $A{-}X$ distance by the $M{-}X$ distance times root square of two:

$$t = \frac{\langle A-X\rangle}{\sqrt{2}\langle B-X\rangle}$$

The deviation of t from 1 is proportional to the structure distortion energy, which is a part of the total energy of a compound. The higher the distortion energy, the less favored is the formation of the perovskite structure. Thus, different tolerance factors of $AMoO_3$ compared to those of the corresponding oxynitrides can explain whether substitution of oxygen with nitrogen leads to the less distorted and thus, more stable structure. Tolerance factors of $CaMo^{4+}O_3$, $SrMo^{4+}O_3$ and $BaMo^{4+}O_3$ calculated from ionic radii of the constituent ions [32,33] are 0.95, 0.98 and 1.03 correspondingly, whereas for the corresponding oxynitrides, for example, $CaMo^{6+}ON_2$, $SrMo^{6+}ON_2$ and $BaMo^{6+}ON_2$ they are equal to 0.97, 1.01 and 1.05. According to these values, the substitution of O^{2-} with N^{3-} in $CaMoO_3$ and $SrMoO_3$ reduces the structure distortion energy. Thus, the substitution is favorable for the perovskite structure formation. On the other hand, for $BaMoO_3$ partial substitution of O^{2-} with N^{3-} would lead to a more distorted structure. Therefore, it can be expected that formation of the phase pure $BaMo(O,N)_3$ at ambient pressure will be difficult, which is in an accordance with our experiments.

It has to be noted that only the tolerance factor consideration, which in many cases is sufficient to compare crystal structures stability of perovskite-type oxides or fluorides (e.g. materials with predominantly ionic type of bonding) may not be enough to compare crystal structure stability of an oxide with that of the corresponding oxynitride. Indeed, higher covalence of the Mo–N bonding as compared to that of the Mo–O bonding makes the $Mo{-}(O,N)_6$ octahedra more flexible to distort. Even if this type of distortion occurs only locally, it may sufficiently reduce structure distortion energy.

It is worth to compare our results on the ammonolysis of $BaMoO_4$ and $BaMoO_3$ with those reported by Liu et al. [11]. Here the formation of the perovskite–oxynitride phase $BaMo(O,N)_3$ during the ammonolysis of both $BaMoO_3$ and $BaMoO_4$ can be observed, while the authors of Ref. [11] reported that they were not able to convert $BaMoO_3$ and $BaMoO_4$ into $BaMo(O,N)_3$. This can be explained by the difference in the ammonia chemical potential which originates from the different ammonia flow used during the studies as discussed above.

So far, only few information on the crystal structure of the perovskite-type $CaMoO_3$ is available in literature. Based on XRPD

data a monoclinic symmetry was proposed for that material [13]. In contrast, de la Calle et al. [14] suggested an orthorhombic symmetry with the space group *Pbnm* based on the results of ND data refinement. An alternative monoclinic symmetry was not yet tested. Most of both $CaMoO_3$ and $CaMo(O,N)_3$ crystallites analyzed by means of selected area ED exhibit complicated ED patterns due to the presence of twin domains. In such a case, different twin orientations superposed by double diffraction make the observation of the extinctions discarding glide planes and screw axis difficult. Here, to choose between the possible space groups X-ray diffraction was used additionally.

Extinction conditions observed on XRPD patterns of both $CaMoO_3$ and $CaMo(O,N)_3$ matched with orthorhombic (*Pbnm*), and monoclinic ($P2_1/n$) unit cells with lattice parameters $\sqrt{2}a_p \times \sqrt{2}a_p \times 2a_p$ and $\sqrt{2}a_p \times 2a_p \times \sqrt{2}a_p$ (a_p = cubic perovskite lattice parameter), respectively. Subsequent Rietveld refinements using these models converged with close values of the fit quality indicators.

ED patterns (Fig. 3 and 4) do exhibit reflections with indices ($h00$), ($0k0$) and ($00l$): $h = 2n+1$, $k = 2n+1$, and $l = 2n+1$. But these reflections are less intense compared to ($h00$), ($0k0$) and ($00l$): $h = 2n$, $k = 2n$, $l = 2n$, and disappear upon the sample rotation. They are therefore to be attributed to double diffraction. This conclusion is also confirmed by the absence of any forbidden diffraction in the [010] zone. On both our XRPD and ED (Fig. 3A) patterns we do not observe ($0kl$) reflections (with $k = 2n+1$), which are allowed in the $P2_1/n$ space group and are not allowed in the space group *Pbnm*. From that we conclude that the true space group for both $CaMoO_3$ and $CaMo(O,N)_3$ is *Pbnm*.

Mainly two types of twin domains were found for $CaMoO_3$: (A) 45° oriented [$\bar{1}\,\bar{1}\,0$] and [001] domains; (B) Domains formed by the superposition of [010] and [100] zone axes.

For $CaMo(O,N)_3$ more twin-domain types have been found: (A) 90° oriented [$\bar{1}\,\bar{1}\,0$] domains (Fig. 4A); (B) 90° oriented [001] domains (Fig. 4B); (C) 60° oriented [$\bar{2}01$] domains (Fig. 4C) (D) 45° oriented [$\bar{1}\bar{1}0$] and [001] domains (Fig. 4D).

Formation of twin domains of these types has been reported earlier for a number of distorted perovskite-type oxides with similar lattice parameters (in our case the mismatch for $CaMoO_3$ between a and b is 2.3%, whereas for $CaMoO_{1.7(1)}N_{1.3(1)}$ the mismatch is 0.9%) [34–37].

Rietveld refinements of $CaMo(O,N)_3$ from both neutron and X-ray data were carried out in space group *Pbnm*. In the starting structural model the Ca:Mo ratio was set to 1:1, whereas the O:N ratio was set to 2:1. The background was determined manually, refined at the initial stages and fixed during the further refinement. Displacement parameters were refined isotropically for all the atoms. Since X-rays are not able to distinguish between O^{2-} and N^{3-}, we did not attempt to refine the anionic composition from the X-ray data. During the neutron data refinement, the occupancy factors for oxygen and nitrogen were refined with the anionic site constrained to be fully occupied. Finally, the lattice and the profile parameters, $2\Theta_0$, the background coefficients, the thermal displacement factors and the anionic occupancies (neutron data) were refined together. To improve the fit, δ-MoN ($P\bar{6}m2$), [38] γ-Mo_2N ($Fm\bar{3}m$), [39] and CaO ($Fm\bar{3}m$) were included in the refinements. The quantities of these secondary phases were determined from the XRPD data (Fig. 5) refinement (the refinement resulted in <1 wt % of CaO and <2 wt % of each MoN and Mo_2N phases) and were kept fixed during the neutron data refinement. Further inspection of the ND profiles and difference graphs revealed evanescent weak features attributed to the presence of a minor impurity phase which could not be identified. Therefore, the regions containing main reflections of that phase were excluded from the refinement.

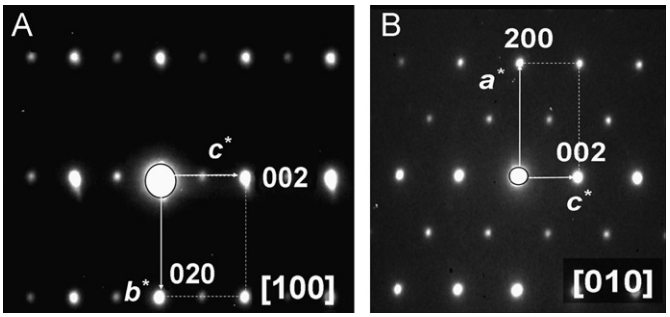

Fig. 3. Electron diffraction patterns for $CaMo(O,N)_3$ taken along the (A) [100] and (B) [010] orthorhombic zone axis.

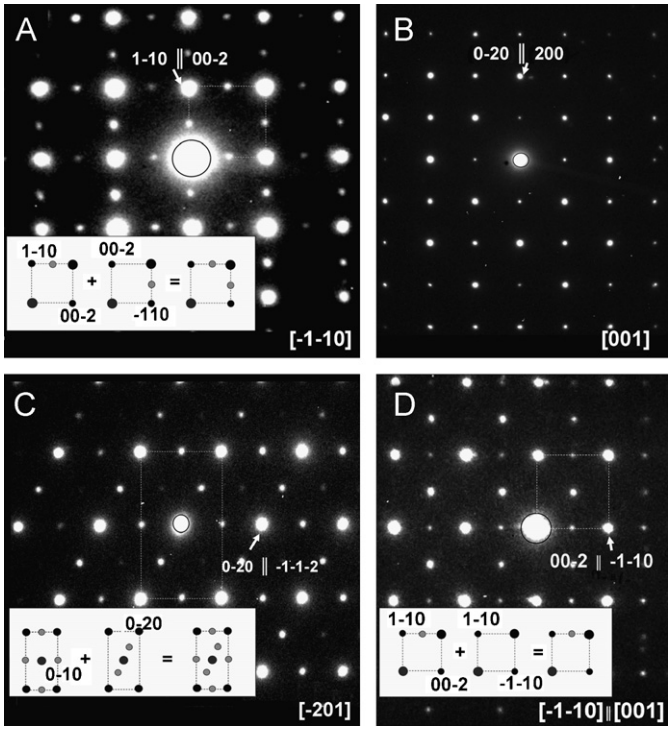

Fig. 4. Examples of ED patterns resulting from the superposition of different twin domains in $CaMo(O,N)_3$: (A) 90° oriented [$\bar{1}\bar{1}0$] domains; (B) 90° oriented [001] domains; (C) 60° oriented [$\bar{2}01$] domains; (D) 45° oriented [$\bar{1}\bar{1}0$] and [001] domains.

The statistics of the refinements, the visual inspection of the fit (Figs. 5 and 6) and the refined values of the displacement parameters indicate that the chosen model was correct. The refined O/N content and the anionic distribution correspond to the composition $CaMoO_{1.7(1)}N_{1.3(1)}$ with a totally disordered O/N arrangement. The result is in good agreement with the hotgas extraction analysis, which yielded in the composition of $CaMoO_{1.79(5)}N_{1.25(2)}$ obtained after subtracting the minor secondary phases contribution (taken from the refinement). The neutron data-derived O/N content corresponds to the formal oxidation state of Mo+5.3. Higher nitrogen content of this phase as compared to that of the $SrMo(O,N)_3$ phase [12] can be explained by higher ammonia flow and lower synthesis temperature employed during the present investigation. As a summary of the refinements, the obtained structural parameters bond lengths and angles are displayed in Tables 1 and 2.

According to the refinements, the average Ca–O/N distance increases upon the substitution of oxygen with nitrogen, which is consistent with a larger ionic radius of N^{3-} (1.48 Å) compared to that of O^{2-}(1.38 Å). The average Mo–O/N distance value of $CaMoO_{1.7(1)}N_{1.3(1)}$ (1.994(2) Å) resembles the one determined for

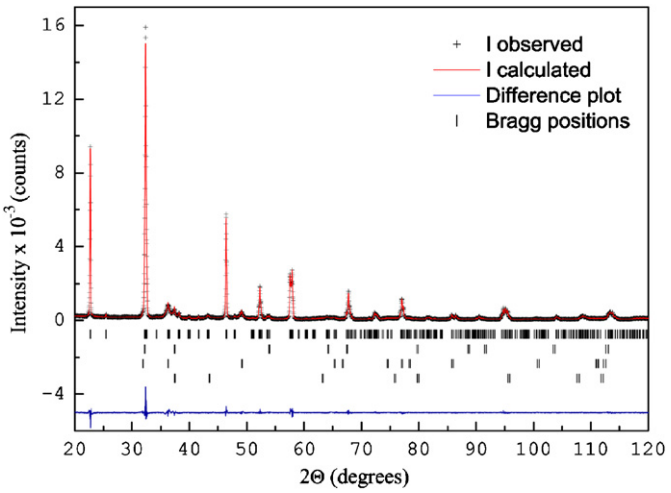

Fig. 5. Rietveld refinement plot of the X-ray powder diffraction data for $CaMoO_{1.7(1)}N_{1.3(1)}$. Space group: *Pbnm*. The observed intensities, calculated profile, difference curve and Bragg positions are shown. CaO, δ-MoN and γ-Mo_2N have been included as a minor impurity phase in the refinement.

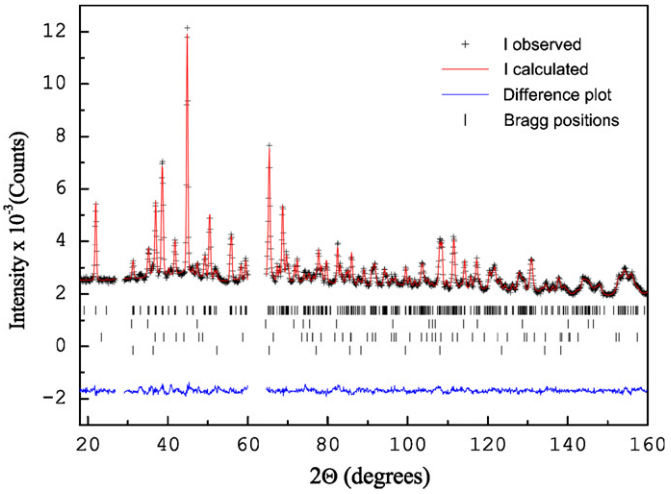

Fig. 6. Rietveld refinement plot of the neutron powder diffraction data for $CaMoO_{1.7(1)}N_{1.3(1)}$. Space group: *Pbnm*. The observed intensities, calculated profile, difference curve and Bragg positions are shown. CaO, δ-MoN and γ-Mo_2N have been included as a minor impurity phase in the refinement.

$SrMoO_{1.89(2)}N_{1.11(2)}$ by ND (1.999(5) Å). [12] However, partial substitution of O^{2-} in $SrMoO_3$ by N^{3-} leads to an increase of the average Mo–O/N distance, which is not the case for $CaMoO_3$ (Table 2), where the mean Mo–O/N distance is not significantly affected by the substitution. Moreover, the smaller average Mo–O/N distance in $CaMoO_{1.7(1)}N_{1.3(1)}$ compared to that in $SrMoO_{1.89(2)}N_{1.11(2)}$ does not completely agree with the O/N composition of these phases. This indicates that $CaMoO_{1.7(1)}N_{1.3(1)}$ may contain anionic/cationic vacancies. Displacement parameters values of Ca and Mo in $CaMoO_{1.7(1)}N_{1.3(1)}$ are higher than those in $CaMoO_3$, which gives a hint for the presence of cationic vacancies in the former compound. Hence true formal oxidation state of Mo in this compound must be slightly lower than that calculated from the O/N content.

Based on the refined Mo–O/N–Mo angle values for $CaMoO_3$ and $CaMoO_{1.7(1)}N_{1.3(1)}$, it can be concluded that the crystal structure of the latter compound is less distorted. This is in accordance with higher ionic radius of N^{3-} compared to that of O^{2-}.

Similar to $CaMoO_3$, the reflections of $CaMoO_{1.7(1)}N_{1.3(1)}$ are broadened isotropically (Fig. 7). The refined apparent size and

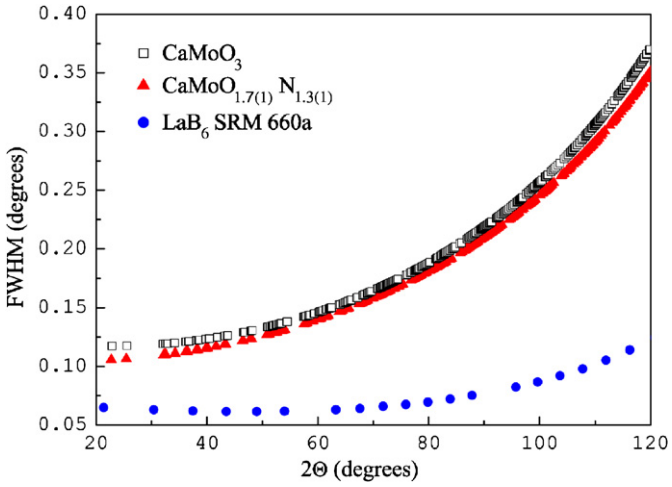

Fig. 7. Angular variation of the total full-width at half-maximum (FWHM) determined from whole profile Rietveld refinements of the XRPD data for $CaMoO_3$, $CaMoO_{1.7(1)}N_{1.3(1)}$ and the standard LaB_6 SRM 660a.

strain values of the latter compound are 0.14 μm and 0.29% which are close to the values obtained for $CaMoO_3$.

Size broadening on the diffractograms can be attributed to both the crystallites size and the presence of twin domains. Small apparent strain values obtained for $CaMoO_3$ as well as for $CaMoO_{1.7(1)}N_{1.3(1)}$ confirm that both materials are chemically homogeneous. The larger apparent size and the smaller apparent strain values obtained for $CaMoO_{1.7(1)}N_{1.3(1)}$ compared to $CaMoO_3$ can arise either from the smaller mismatch between *a* and *c* lattice constants for the former compound or from the different thermal history of the samples, which would also explain the multiplicity of different twin types observed for $CaMoO_{1.7(1)}N_{1.3(1)}$ by TEM.

Since no apparent reflection splitting was noticed on the XRPD pattern of $BaMo(O,N)_3$ and its main reflections were isotropically broadened, we assign its space group as $Pm\bar{3}m$. This confirms its totally disordered anionic arrangement. XRPD reveals a crystallite size of $BaMo(O,N)_3$ (0.12 μm) similar to that of $CaMo(O,N)_3$ which was in accordance with electron microscopy studies. Because of the unknown impurity composition and structure, we did not attempt a whole pattern refinement of XRPD data of $BaMo(O,N)_3$, but rather estimate the lattice constant and line broadening of $BaMo(O,N)_3$. The obtained lattice constant (4.0657(1) Å) is larger than the one refined from the XRPD data for $BaMoO_3$ (4.0409(1) Å). Contrary to the partial oxidation of Mo^{4+} to smaller Mo^{5+} and Mo^{6+}, a partial replacement of O^{2-} with larger N^{3-} will lead to the increase of the lattice constant. From the comparison of the lattice constant values for $BaMoO_3$ and $BaMo(O,N)_3$ it follows that it is the difference in the ionic radii of O^{2-} and N^{3-}, which has a major influence on the lattice constant. The larger lattice constant of $BaMo(O,N)_3$ indicates that both Mo–O/N and Ba–O/N distances increase upon partial substitution of O^{2-} with N^{3-} in $BaMoO_3$.

4. Conclusions

The possibilities to prepare previously unreported oxynitride–perovskite $AMo(O,N)_3$ (A = Ca, Ba) phases by thermal ammonolysis of $AMoO_4$ and $AMoO_3$ oxide precursors were successfully investigated.

Only the ammonolysis of $CaMoO_3$ and $BaMoO_3$ led to a considerable yield of the desired phases. $CaMoO_4$ decomposes to

CaO and Mo_2N when reacted with ammonia. $BaMo(O,N)_3$ is formed as a minor phase during the ammonolysis of $BaMoO_4$, which yields mainly in $Ba_3Mo_2O_6N_2$. Thus, the crystal structure of the starting precursor is crucial for the desired phase formation. As the other factors influencing the phase formation during the ammonolysis of $AMoO_3$ and $AMoO_4$ the gas to solid ratio, positive inductive effect of the *A*-site cation, the lattice energy, the structure distortion energy and Mo–N bonding covalence were considered.

$CaMo(O,N)_3$ crystallizes in space group *Pbnm* and possesses a less distorted crystal structure than $CaMoO_3$. ND reveals a statistical distribution of O^{2-} and N^{3-} among the available anionic sites and an anionic content corresponding to the composition $CaMoO_{1.7(1)}N_{1.3(1)}$.

TEM shows evidence for twin domains in both $CaMoO_3$ and $CaMoO_{1.7(1)}N_{1.3(1)}$, which together with the average crystallite size may be responsible for the line profile broadening in the XRPD patterns. The multiplicity of different twin types measured for $CaMoO_{1.7(1)}N_{1.3(1)}$ compared to $CaMoO_3$ can be explained on the one hand by the smaller mismatch between *a* and *c* lattice constants in the former compound or on the other hand by the different thermal history of the compounds.

$BaMo(O,N)_3$ adopts the space group $Pm\bar{3}m$. This indicates a completely disordered O/N arrangement as found for $CaMoO_{1.7(1)}N_{1.3(1)}$. Its determined lattice parameter and consequently both Mo–O/N and Ba–O/N distances are larger than those of the corresponding $BaMoO_3$ as revealed by X-ray diffraction. This finding is attributed to the larger ionic radius of N^{3-} compared to that of O^{2-}.

Thus, as future work, studies on thermal reoxidation and catalytic properties of the synthesized phases are planned.

Acknowledgments

The authors acknowledge the German Science Foundation (DFG-SPP 1136) and Empa for the financial support and Dr. Denis Sheptyakov (SINQ, Paul Scherrer Institute) for the technical assistance. This work is partly based on the experiments performed at the Swiss Spallation Neutron Source SINQ, Paul Scherrer Institute, Villigen, Switzerland.

Appendix A. Supplementary Materials

Supplementary data associated with this article can be found in the online version at doi:10.1016/j.jssc.2008.05.012.

References

[1] W.E. Newton, Philos. Trans. R. Soc. Lond. B 317 (1987) 259–277.
[2] D. McKay, J.S.J. Hargreaves, J.L. Rico, J.L. Rivera, X.L. Sun, J. Solid State Chem. 181 (2008) 325–333.
[3] L. Le Gendre, R. Marchand, Y. Laurent, J. Eur. Ceram. Soc. 17 (1997) 1813–1818.
[4] R. Marchand, Y. Laurent, J. Guyader, P. L'Haridon, P. Verdier, J. Eur. Ceram. Soc. 8 (1991) 197–213.
[5] F. Tessier, R. Marchand, J. Solid State Chem. 171 (2000) 143–151.
[6] A. Rachel, S.G. Ebbinghaus, M. Gungerich, P.J. Klar, J. Hanss, A. Weidenkaff, A. Reller, Thermochim. Acta 438 (2005) 134–143.
[7] R. Marchand, F. Pors, Y. Laurent, Ann. Chim. Fr. 16 (1991) 553–560.
[8] P. Antoine, R. Marchand, Y. Laurent, C. Michel, B. Raveau, Mater. Res. Bull. 23 (1988) 953–957.
[9] I.D. Fawcett, K.V. Ramanujachary, M. Greenblatt, Mater. Res. Bull. 32 (1997) 1565–1570.
[10] P. Maillard, F. Tessier, E. Orhan, F. Chevire, R. Marchand, Chem. Mater. 17 (2005) 152–156.
[11] G. Liu, X. Zhao, H.A. Eick, J. Alloys Compd. 187 (1992) 145–156.
[12] D. Logvinovich, R. Aguiar, R. Robert, M. Trottmann, S.G. Ebbinghaus, A. Reller, A. Weidenkaff, J. Solid State Chem. 180 (2007) 2649–2654.
[13] K. Kamata, T. Nakamura, T. Sata, Chem. Lett. 4 (1975) 81–86.
[14] C. de la Calle, J.A. Alonso, M. Garcia-Hernandez, V. Pomjakushin, J. Solid State Chem. 179 (2006) 1636–1641.
[15] L.H. Brixner, J. Inorg. Nucl. Chem. 14 (1960) 225–230.
[16] K. Kamata, T. Nakamura, T. Sata, Mater. Res. Bull. 10 (1975) 373–378.
[17] Z. Singh, S. Dash, R. Prasad, D.D. Sood, J. Alloys Compd. 215 (1994) 303–307.
[18] D. Logvinovich, A. Borger, M. Dobeli, S.G. Ebbinghaus, A. Reller, A. Weidenkaff, Prog. Solid State Chem. 35 (2007) 281–290.
[19] P. Thompson, D.E. Cox, J.B. Hastings, J. Appl. Crystallogr. 20 (1987) 79–83.
[20] B. van Laar, W.B. Yelon, J. Appl. Crystallogr. 17 (1984) 47–54.
[21] L.W. Finger, D.E. Cox, A.P. Jephcoat, J. Appl. Crystallogr. 27 (1994) 892–900.
[22] J. Rodriguez-Carvajal, T. Roisnel, Mater. Sci. Forum 443–444 (2004) 123–126.
[23] P. Fischer, G. Frey, M. Koch, M. Konnecke, V. Pomjakushin, J. Schefer, R. Thut, N. Schlumpf, R. Burge, U. Greuter, Physica B 276–278 (2000) 146–147.
[24] J. Rodriguez-Carvajal, Physica B 192 (1993) 55–69.
[25] P.A. Stadelmann, Ultramicroscopy 21 (1987) 131–145.
[26] M.T. Weller, S.J. Skinner, Int. J. Inorg. Mater. 2 (2000) 463–467.
[27] P. Subramanya Herle, M.S. Hegde, G.N. Subbanna, J. Mater. Chem. 7 (1997) 2121–2125.
[28] P. Ettmayer, Monatshefte Chem./Chem. Monthly 101 (1970) 127–140.
[29] S.H. Elder, F.J. DiSalvo, L. Topor, A. Navrotsky, Chem. Mater. 5 (1993) 1545–1553.
[30] S.J. Clarke, K.A. Hardstone, C.W. Michie, M.J. Rosseinsky, Chem. Mater. 14 (2002) 2664–2669.
[31] J. Etourneau, J. Portier, F. Menil, J. Alloys Compd. 188 (1992) 1–7.
[32] R.D. Shannon, C.T. Prewitt, Acta Crystallogr. B 25 (1969) 925–946.
[33] R. Shannon, Acta Crystallogr. A 32 (1976) 751–767.
[34] Y. Wang, R.C. Liebermann, Phys. Chem. Miner. 20 (1993) 147–158.
[35] H. Nakano, M. Kobayashi, N. Kamegashira, J. Am. Ceram. Soc. 90 (2007) 1276–1279.
[36] A. Weidenkaff, M.H. Aguirre, T. Lippert, U. Falke, U. Bangert, Chimia 60 (2006) 742–748.
[37] M.H. Aguirre, R. Robert, D. Logvinovich, A. Weidenkaff, Inorg. Chem. 46 (2007) 2744–2750.
[38] C.L. Bull, P.F. McMillan, E. Soignard, K. Leinenweber, J. Solid State Chem. 177 (2004) 1488–1492.
[39] T. Kawashima, E. Takayama-Muromachi, P.F. McMillan, Physica C 460–462 (2007) 651–652.